

# Effects of supersonic fine particle bombardment on the microstructure and properties of an Mg-1.8Zn-0.5Zr-1.5Gd biological magnesium alloy

Yao Huai<sup>1,2\*</sup>, Yuhui Wang<sup>1</sup>, Shubo Wang<sup>3</sup>, Yi Xiong<sup>1</sup>, Marko Huttula<sup>3,1</sup>, Wei Cao<sup>3</sup>

<sup>1</sup>*School of Materials Science and Engineering, Henan University of Science and Technology, Luoyang Henan 471023, P. R. China*

<sup>2</sup>*Collaborative Innovation Center of Nonferrous Metals of Henan Province, Luoyang Henan 471023, P. R. China*

<sup>3</sup>*Nano and Molecular Systems Research Unit, Centre for Advanced Steels Research, University of Oulu, FI-90014, Finland*

Received 18 April 2023, received in revised form 8 May 2023, accepted 22 May 2023

## Abstract

With the help of supersonic fine particle bombardment technology, a gradient nanostructure with a certain layer depth was constructed on the surface of an Mg-1.8Zn-0.5Zr-1.5Gd biological magnesium alloy. The effects of bombardment time on the microstructure, mechanical properties, and corrosion resistance of the gradient nanostructure were investigated. The results showed that the layer depth and surface roughness of the gradient nanostructures increased with an increase in the bombardment time, and the corresponding mechanical properties and corrosion resistance first increased and then decreased with an extension of the bombardment time. When the bombardment time was 30 s, the alloy had good mechanical properties and corrosion resistance. Its tensile strength, yield strength, elongation, and static corrosion rate were  $299.1 \pm 2.2$  MPa,  $264.4 \pm 1.5$  MPa,  $36.8 \pm 1.3$  %, and  $0.307 \pm 0.015$  mm y<sup>-1</sup>, respectively. The results of the 120-h immersion experiment in simulated human body fluids showed that the average corrosion rate of the alloy first decreased, then increased, and finally decreased with an extension of the immersion time and finally tended to stabilize.

**Key words:** biological magnesium alloy, supersonic fine particle bombardment, microstructures, corrosion resistance

## 1. Introduction

As a biodegradable implant material, magnesium alloys have good biocompatibility with the human body, and their mechanical properties are close to those of human bone (the elastic modulus of magnesium alloys is 41–45 GPa, and the elastic modulus of human bone is 3–20 GPa). This effectively avoids the stress shielding effect caused by the large differences in their mechanical properties. The magnesium ions released by the biological magnesium alloy used as a graft material can promote the formation of calcium deposits and phosphate substances around the damaged tissue. Therefore, it also accelerates the generation of osteoblasts and new bone around the damaged

tissue, thus promoting the healing of the damaged tissue. As a result, in the field of medical biomaterials, magnesium alloys have attracted the attention of researchers [1–3].

Although magnesium alloys have many advantages, they are challenging in clinical applications as medical implant materials. Because of the stress of action, the degradation rate of magnesium alloys in the human environment will be faster [4]. This faster degradation rate will easily lead to the loss of the integrity of the mechanical properties of the graft material before the damaged tissue heals. At the same time, it will also lead to an increase in the surrounding pH value of the graft material, which, in turn, affects the healing of the tissue to be repaired [5]. Therefore, bi-

\*Corresponding author; e-mail address: [yaohuaitougao@126.com](mailto:yaohuaitougao@126.com)

ological magnesium alloy graft materials must meet certain criteria regarding mechanical properties and corrosion resistance. Magnesium alloy materials used in cardiovascular stents must meet two prerequisites: the yield strength (YS) must be greater than 200 MPa, and the elongation (EL) must be over 20 %. For magnesium alloy materials used for the internal fixation of fractures, the YS and EL must be greater than 200 MPa and 10 %, respectively. At the same time, when these alloys are immersed in simulated body fluid (SBF) at 37 °C for 120 h, the mode of corrosion must be uniform, and the average corrosion rate must be less than 0.5 mm y<sup>-1</sup> [6]. An ideal magnesium alloy graft material should have a slow degradation rate in the early stage to provide sufficient strength to achieve fixed support. In the later stage, the mechanical properties of the implant material should be gradually reduced, and the load should be transferred to the new bone tissue, followed by complete degradation. Currently, most magnesium alloys cannot achieve these goals [7]. Insufficient strength and toughness, localized corrosion, high degradation rates, and uncontrollable degradation are the main challenges to the development and application of medical magnesium alloys.

Refining the grain of magnesium alloys and constructing gradient nanocrystalline layers on the surface can improve the corrosion resistance and mechanical properties of magnesium alloys. At the same time, the degradation rate can also be controlled by changing the thickness of the nanocrystalline layers [8, 9]. The grain size of an Mg-2.0Zn-0.5Zr-3.0Gd magnesium alloy was reduced from 150 to about 5 µm by hot extrusion deformation. The YS and EL were increased by 32.6 and 138.4 %, respectively, and the corrosion rate decreased by 23.2 % after hot extrusion deformation [10]. The grain size of the Mg-1.0Zn-0.6Zr-5.0Gd magnesium alloy decreased from 50 µm before extrusion to about 5 µm; its YS and EL increased by 100 and 108.9 %, respectively, and the corrosion rate decreased by 59.3 % [11]. A gradient nanostructure was constructed on the surface of an Mg-4%Y-3.3%RE(Nd,Gd)-0.5%Zr magnesium alloy by supersonic fine particle bombardment (SFPB) technology, which improved compressive and bending properties of the alloy by 18.2 and 23.1 %, respectively, and the corrosion rate decreased by 29.2 %, indicating that the mechanical properties and corrosion resistance were significantly improved [12]. Through the SFPB treatment of the surface of AZ31 and AZ91 alloys, nanocrystalline layers of about 103 and 120 nm were obtained on the surface of the alloys, and their hardness and corrosion resistance were greatly improved [13]. These research results show that grain refinement and surface nano treatment can improve the mechanical properties and corrosion resistance of magnesium alloys.

According to the principle of biosafety [14], based

on previous work, the author developed an Mg-1.8Zn-0.5Zr-1.5Gd alloy with a low Gd content and improved its mechanical properties and corrosion resistance by reverse extrusion technology. However, the corrosion resistance of the as-extruded alloy decreased with an increase in the immersion time. In order to overcome these shortcomings, this study intended to use the SFPB technology as a surface nano treatment of the as-extruded alloy. The influence of the bombardment time on the microstructure, mechanical properties, and corrosion resistance of the extruded alloy was studied. The change law of the degradation rate and the corrosion mechanism of different immersion times are discussed, to provide experimental and technical support for developing a medical magnesium alloy that meets the mechanical properties and corrosion resistance and a controllable corrosion rate.

## 2. Experimental procedure

The raw materials used for smelting the alloys were magnesium ingots with a purity greater than 99.9 %, zinc ingots, Mg-20%Gd, and Mg-25%Zr master alloys. The alloy was smelted in a ZGJL0.01-40-4 intermediate frequency induction furnace. The melting temperature and holding time were 780 ± 5 °C and 20 min, respectively, and the casting temperature was 720 ± 5 °C. The molten alloy was solution-treated at 470 °C for 10 h and then processed into a  $\phi$  50 mm × 35 mm ingot for extrusion. Before extrusion, the extrusion die and the ingot to be extruded were kept at 350 °C for 2 h, and the extrusion ratio and extrusion rate were 7.7 and 5 mm s<sup>-1</sup>, respectively. The annealing treatment was carried out at a temperature of 200 °C for 4 h. We cut a thin plate sample with a size of 210 mm × 160 mm × 4 mm parallel to the direction of extrusion, and ground and polished the plate sample. These samples were then subjected to SFPB for 0, 10, 20, 30, 40, and 50 s, designated as  $E_0$ ,  $E_{10}$ ,  $E_{30}$ ,  $E_{40}$ , and  $E_{50}$ , respectively. The bombardment distance was 10 mm, the gas pressure was 0.5 MPa, and the size of the hard Al<sub>2</sub>O<sub>3</sub> particles used was 50 µm.

We used a metallographic microscope, a JSM-5610LV electron microscope and its accompanying energy-dispersive spectrometer (EDAX), and a JEM-2100 transmission electron microscope to observe the microstructure of the sample and the composition of the micro-area, and to analyze the phase structure. TEM specimens were prepared using a dual-beam FIB-SEM (FEI Scios 2). The distance between the TEM specimen and the nano treatment surface was measured using an SEM image. A Nanovea HS1000P three-dimensional surface topography instrument was used to test the three-dimensional topography of the samples' surface, and the three-dimensional surface

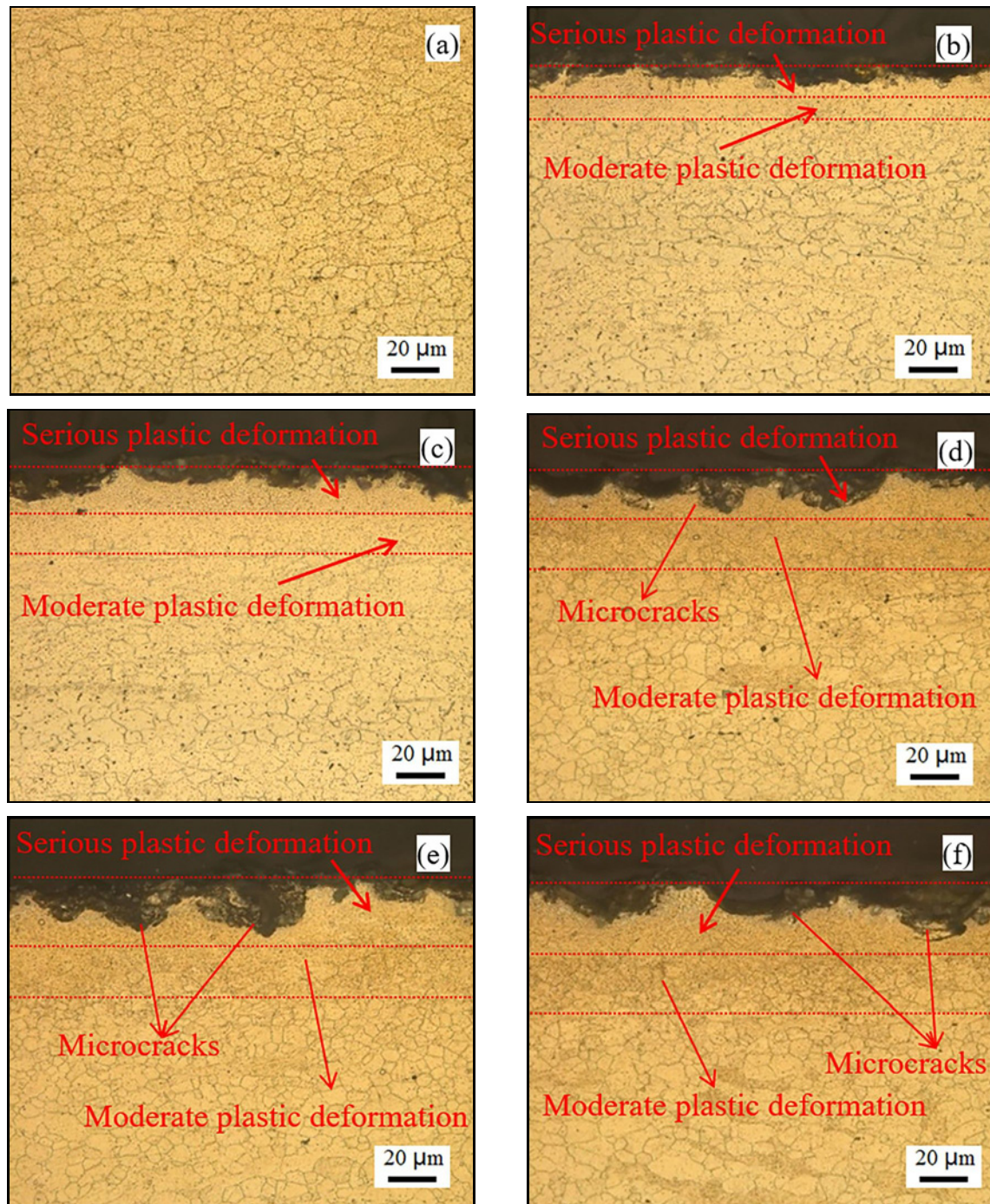


Fig. 1. Optical microstructures of the cross-section of the Mg-1.8Zn-0.5Zr-1.5Gd alloys before and after SFPB: (a)  $E_0$ , (b)  $E_{10}$ , (c)  $E_{20}$ , (d)  $E_{30}$ , (e)  $E_{40}$ , and (f)  $E_{50}$ .

roughness  $S_a$  was calculated. The wire-cutting method was used to cut the tensile specimen parallel to the direction of the extrusion. The size of the length gauge was 40 mm (length)  $\times$  4.5 mm (width)  $\times$  2.0 mm (height). Tensile tests were performed based on the ASTM E8M-09 standard at a crosshead speed of 1 mm  $\text{min}^{-1}$  using an Instron 5587 testing machine. An average of at least three measurements was taken for each group.

A corrosion test was carried out in SBF at 37°C [15]. The samples with a dimension of  $\phi$  18 mm  $\times$  5 mm were immersed in 180 mL SBF. The SBF solution was refilled every 8 h to keep a constant pH value. After the corrosion experiments, the corrosion products of the sample surface were removed using a solution of 20%  $\text{CrO}_3$  + 1%  $\text{AgNO}_3$ . The methods of calculating the corrosion rate of mass loss ( $\text{mm y}^{-1}$ ) and the corrosion rate of hydrogen evolution ( $\text{mm y}^{-1}$ ) are shown

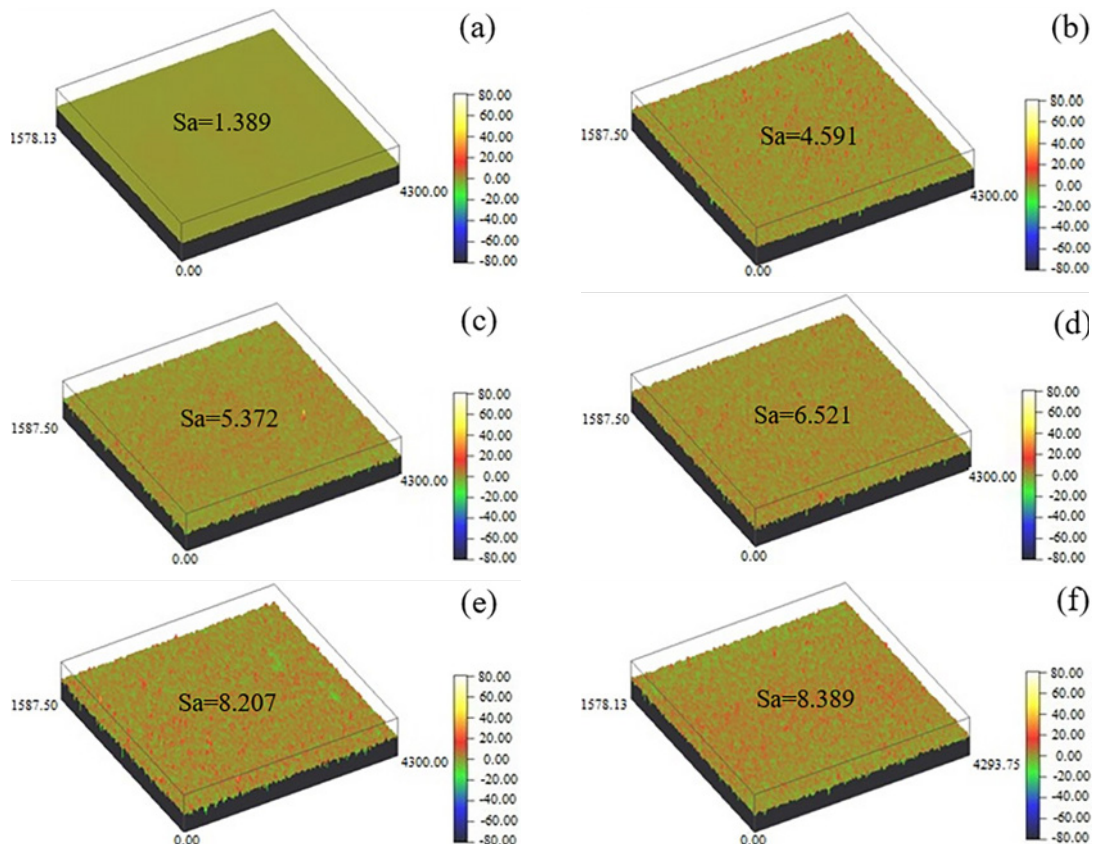


Fig. 2. The three-dimensional morphology of the Mg-1.8Zn-0.5Zr-1.5Gd alloy's surface subjected to SFPB: (a)  $E_0$ , (b)  $E_{10}$ , (c)  $E_{20}$ , (d)  $E_{30}$ , (e)  $E_{40}$ , and (f)  $E_{50}$ .

in Eqs. (1) and (2) [16, 17]:

$$\nu_w = 87.6\Delta m/(\rho At), \quad (1)$$

$$\nu_H = 95.36V_H/(\rho At), \quad (2)$$

where  $\Delta m$  represents the mass loss of the test sample (mg),  $\rho$  represents the density of the test sample ( $\text{g cm}^{-3}$ ),  $A$  represents the surface area of the test sample ( $\text{cm}^2$ ),  $t$  represents the soaking time (h), and  $V_H$  represents the volume of hydrogen collected (mL).

An electrochemical workstation (Autolab PG-STAT128N) and a three-electrode system were used to test the polarization curve of the alloy. The samples to be tested ( $\varnothing 11.3 \text{ mm} \times 5 \text{ mm}$ ), graphite, and saturated calomel electrodes were the working, auxiliary, and reference electrodes, respectively. After immersion of the samples in SBF at  $37^\circ\text{C}$  for 1 h, the polarization curve was tested at the open-circuit potential of  $-0.25$  to  $0.45 \text{ V}$  at a test rate of  $1 \text{ mV s}^{-1}$ .

### 3. Results

#### 3.1. Microstructure

Figure 1 shows the metallographic microstructure of the extruded Mg-1.8Zn-0.5Zr-1.5Gd alloy before

and after SFPB. It can be seen from Fig. 1a that the as-extruded Mg-1.8Zn-0.5Zr-1.5Gd alloy underwent complete dynamic recrystallization, and the alloy's structure was obviously refined. The average grain size was about  $7.3 \mu\text{m}$ . Figures 1b–f show the metallographic structure of the alloy's cross-section after bombardment at different times. It can be seen from the figure that the SFPB caused serious plastic deformation in the surface layer of the alloy, and the thickness of the serious plastic deformation layer increased with an increase in the bombardment time. The equiaxed grains disappeared completely, and the thickness of the corresponding moderate plastic deformation layer also increased, and the equiaxed grains showed the characteristics of elongated deformation. When the bombardment time was longer than 30 s, obvious microcracks began to appear on the surface of the alloy, and the depth of the surface cracks gradually increased with an increase in the bombardment time.

The three-dimensional morphology and surface roughness of the as-extruded Mg-1.8Zn-0.5Zr-1.5Gd alloy's surface after SFPB for different times are shown in Fig. 2. Different colors represent the depth of the three-dimensional morphology, and a greater color span indicates that the surface roughness was greater. As shown in Fig. 2a, the surface of the alloy without

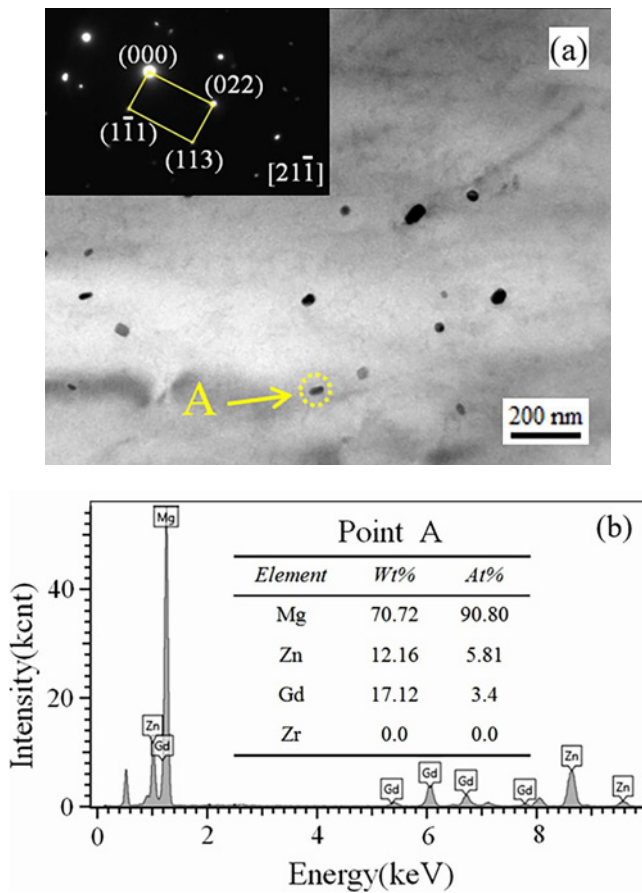


Fig. 3. TEM images and the corresponding SAED patterns and EDS of the second phase of the  $E_{30}$  alloy at 100  $\mu\text{m}$  below the surface.

SFPB was relatively flat, with only small scratches remaining after surface burnishing, and its three-dimensional surface roughness  $Sa$  was only 1.389  $\mu\text{m}$ . After different bombardment times, the alloy's surface underwent different degrees of plastic deformation under the bombardment by high-energy particles, resulting in a certain number of impact craters. As shown in Figs. 2b–f, the surface roughness gradually increased with an increase in the bombardment time, and the surface roughness  $Sa$  reached 8.389  $\mu\text{m}$  after 50 s of SFPB. Usually, when magnesium alloys undergo SFPB for a long time, micro-cracks will appear as the surface roughness of the alloys increases [18].

Figure 3 shows the transmission electron microscopy (TEM) images, the selected area electron diffraction (SAED) patterns, and the energy-dispersive spectrometry (EDS) spectrum at 100  $\mu\text{m}$  below the surface of the  $E_{30}$  alloy. It can be seen from Fig. 3a that a small number of nanoscale second-phase particles are distributed in the alloy. SAED spot (Fig. 3a) calibration and EDS (Fig. 3b) analysis were performed on the nano-sized particles at Point A in

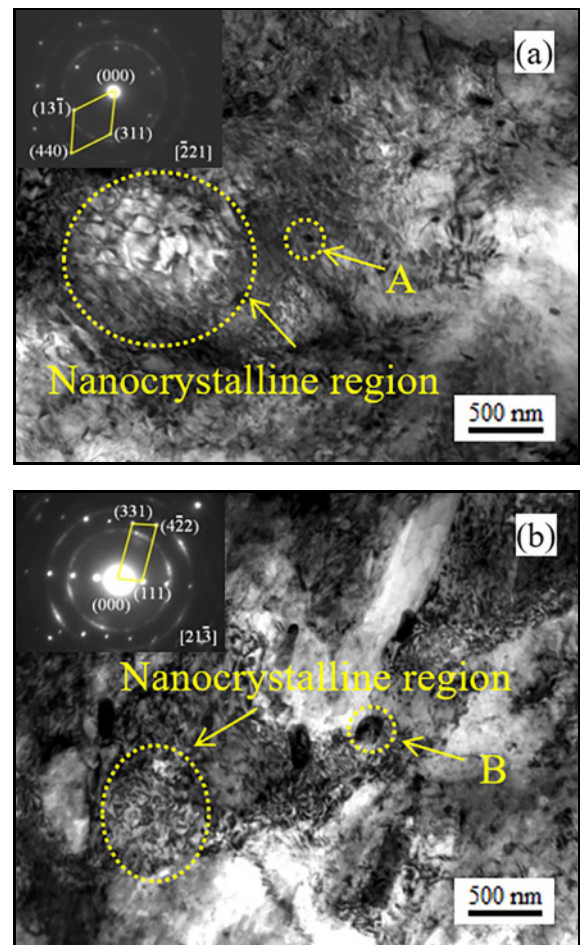


Fig. 4. TEM images and the corresponding SAED patterns of the  $E_{30}$  (a) and  $E_{50}$  (b) alloys at 20  $\mu\text{m}$  below the surface.

Fig. 3a, confirming that the second phase particles belonged to the face-centered cubic structure. The SAED patterns had an interplanar spacing of 0.4214, 0.2193, and 0.2576 nm, respectively, with standard  $\text{Mg}_3\text{Gd}$  in the  $(1\bar{1}1)$ ,  $(113)$ , and  $(022)$  crystal planes. The spacing had a good corresponding relationship with the zone axis  $[21\bar{1}]$ . In addition, the particles were mainly composed of elemental Mg, Zn, and Gd. Therefore, it is inferred that the nano-sized second-phase particles are  $(\text{Mg}, \text{Zn})_3\text{Gd}$  phase particles [19].

It can also be seen from Fig. 3a that the alloy's structure was not deformed, and the second-phase particles were not broken. At the same time, there were no dislocations in the alloy's matrix. Usually, after a magnesium alloy pass undergoes SFPB, the energy generated by the bombardment with high-energy particles will be continuously absorbed and attenuated in the process of passing through the surface and sub-surface of the alloy. Therefore, it can be assumed that when the bombardment time was 30 s, the energy was transmitted to the bottom of the surface, and the bombardment energy at 100  $\mu\text{m}$  was small.

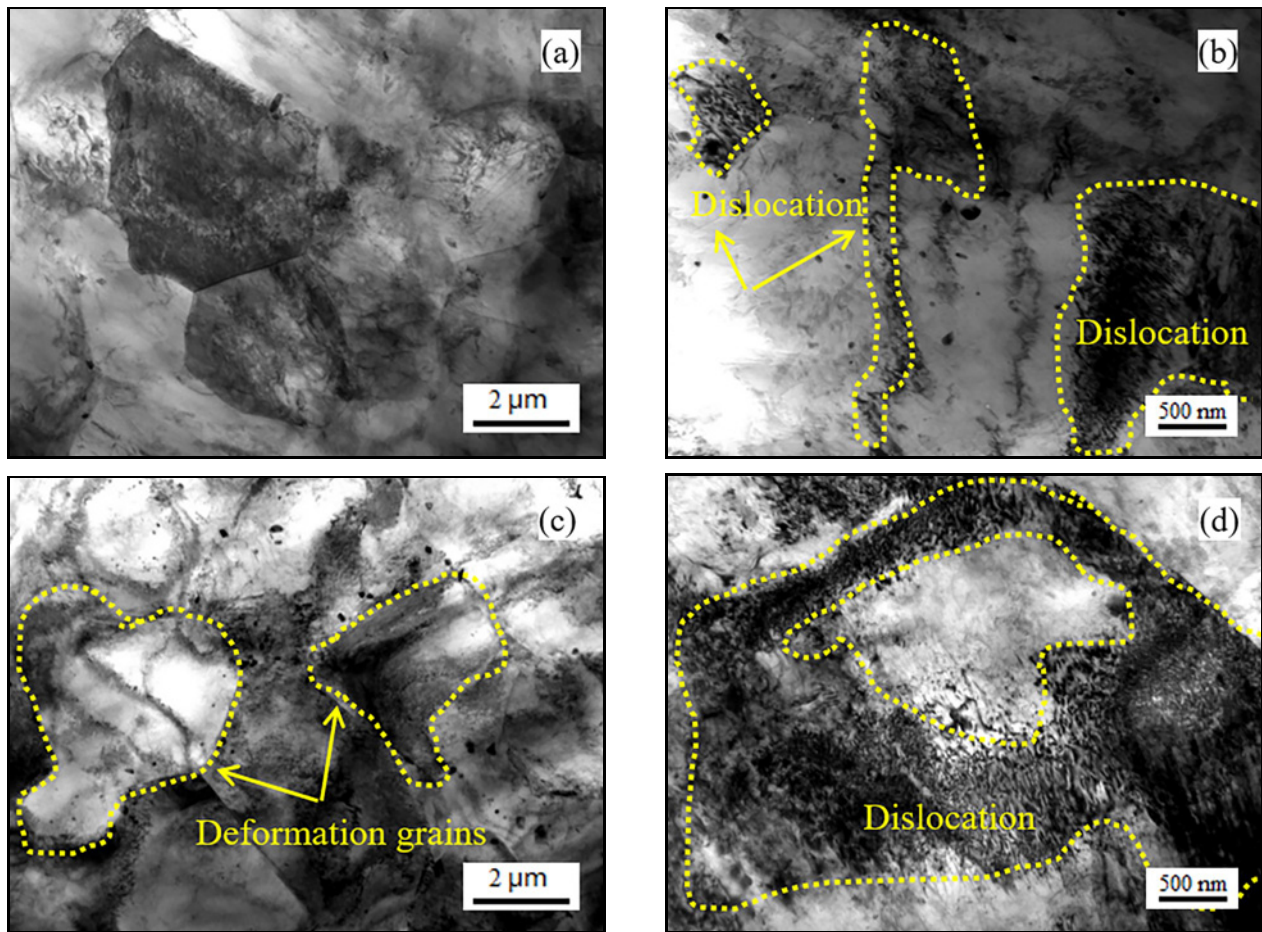


Fig. 5. TEM images of the (a), (b)  $E_{30}$  and (c), (d)  $E_{50}$  alloys at  $35\ \mu\text{m}$  below surface.

Figure 4 shows the TEM images and corresponding SAED spectra at  $20\ \mu\text{m}$  below the surface of the  $E_{30}$  and  $E_{50}$  alloys. As shown in Figs. 4a,b, at  $20\ \mu\text{m}$  below the surface of the  $E_{30}$  and  $E_{50}$  alloys, randomly oriented nanograin regions appeared, and there were a large number of high-density dislocations in the alloys. Meanwhile, the SAED spectra in Areas A and B showed diffraction rings with different degrees of completeness, proving that both regions consisted of nanocrystals with random grain orientation. The integrity of the diffraction ring in Area B is higher, indicating that the degree of nanometerization was higher.

After SFPB, the microstructural changes in the Mg-1.8Zn-0.5Zr-1.5Gd alloy can be considered to be as described by [20–22]. First, the surface area of the alloy will undergo preliminary plastic deformation, and deformation twinning will start under the action of compressive stress, forming twins. At the same time, the lattice distortion intensifies, resulting in an increase in the amount of nucleation and refinement of the grains. With the continuous impact of  $\text{Al}_2\text{O}_3$  particles, serious plastic deformation occurs on the surface of the alloy, and high-density dislocation networks, dislocation tangles, dislocation cells, and dislocation

arrays are generated in the deformed structure. Finally, with the aggravation of the distortion, the deformation caused by energy storage increases, which is conducive to the slips, plug products, and reorganization of the dislocation. This leads to the accumulation, annihilation, appreciation, and rearrangement of the dislocations, which gradually evolve into small-angle grain boundaries and transform into large-angle grain boundaries by constantly absorbing a moving dislocation. The formation process is shown in Fig. 4. The new nanocrystals had a random orientation, a uniform distribution, and clear crystal boundaries, and no absorbed dislocations remained in the alloy matrix. Because of the long bombardment time of the  $E_{50}$  alloy, the nanostructure at  $20\ \mu\text{m}$  below the surface of the alloy was higher.

Figure 5 shows the TEM images at  $35\ \mu\text{m}$  below the surface of the  $E_{30}$  and  $E_{50}$  alloys. It can be seen from Figs. 5a,c that the grains at  $35\ \mu\text{m}$  below the surface of  $E_{30}$  alloy are regularly shaped micron-scale dynamic recrystallization grains, whereas the dynamic recrystallization grains at  $35\ \mu\text{m}$  below the surface layer of the  $E_{50}$  alloy were less deformed by the influence of SFPB. At the same time, a large number of dis-

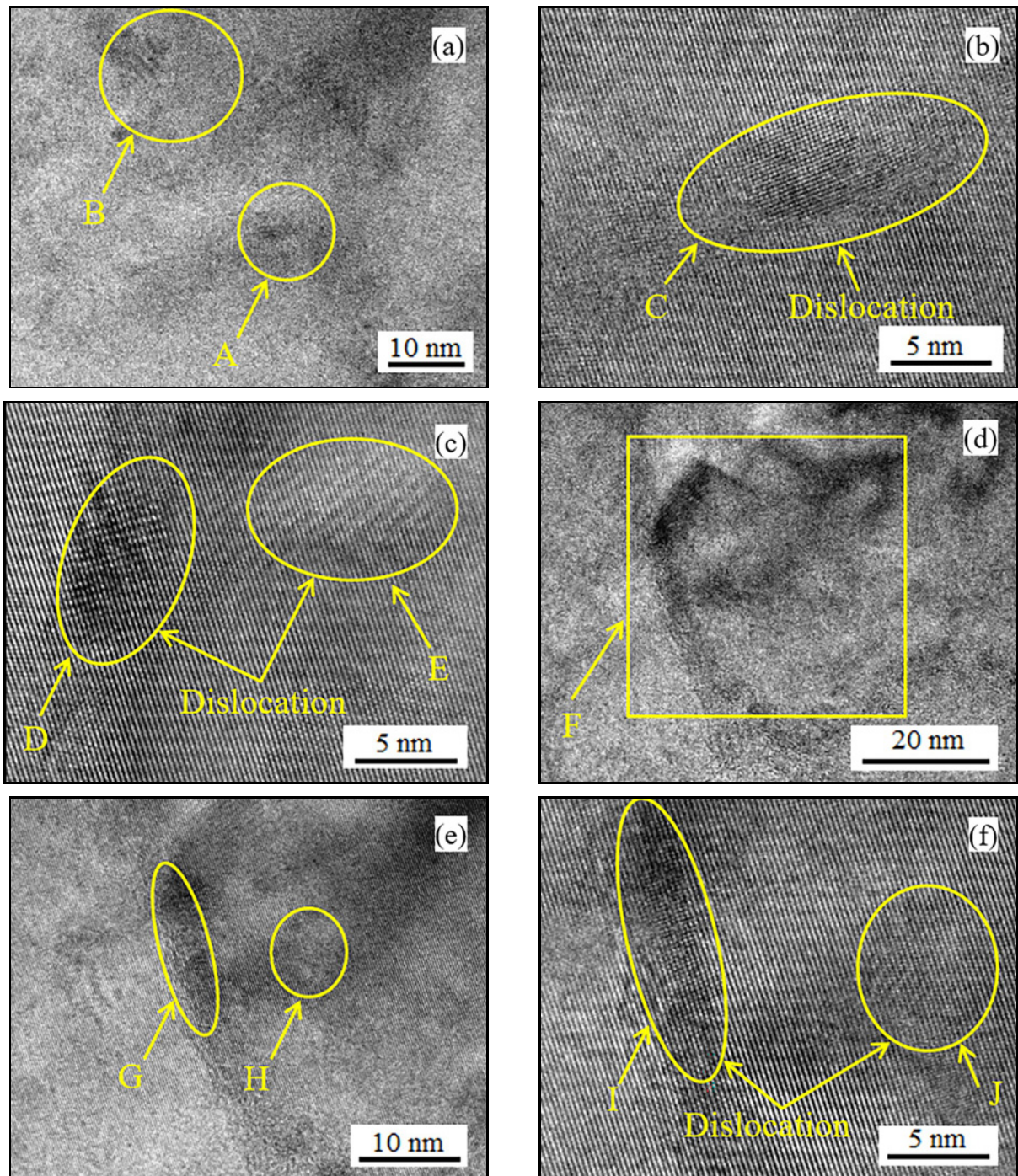


Fig. 6. Typical TEM and HRTEM images of  $E_{30}$  alloys at 35  $\mu\text{m}$  below the surface.

locations accumulated in some regions at 35  $\mu\text{m}$  below the surface of both the  $E_{30}$  and  $E_{50}$  alloys (Figs. 5b,d). However, compared with dislocations at 20  $\mu\text{m}$  below the surface (Fig. 4), both the dislocation density and the area of the dislocation region are reduced significantly. This showed that after the absorption, transfer, and accumulation of the alloy's surface layer, the energy of the bombardment energy could not break the original grain at 35  $\mu\text{m}$  below the alloy surface layer, but it caused high-density dislocations in some

regions. When the bombardment time lengthened, the deformation energy on the alloy's surface increased, and the deformation layer was deeper. Therefore, compared with the  $E_{30}$  alloy, the grain at 35  $\mu\text{m}$  below the surface layer of the  $E_{50}$  alloy had a larger deformation, and the area and density of the dislocation zone were also higher.

Figure 6 shows the TEM image and high-resolution TEM (HRTEM) images of a part of the area 35  $\mu\text{m}$  below the surface of the  $E_{30}$  alloy. Figures 6b,c show

Table 1.  $E_{\text{corr}}$ ,  $I_{\text{corr}}$ , and  $P_i$  of alloys subjected to SFPB for different times, derived from the polarization curves

Material	$E_0$	$E_{10}$	$E_{20}$	$E_{30}$	$E_{40}$	$E_{50}$
$E_{\text{corr}}$ V vs. SCE	$-1.275 \pm 0.005$	$-1.265 \pm 0.005$	$-1.258 \pm 0.005$	$-1.251 \pm 0.005$	$-1.281 \pm 0.005$	$-1.289 \pm 0.005$
$I_{\text{corr}}$ ( $\mu\text{A cm}^{-2}$ )	$2.478 \pm 0.005$	$2.471 \pm 0.005$	$2.467 \pm 0.005$	$2.462 \pm 0.005$	$2.487 \pm 0.005$	$2.495 \pm 0.004$
$P_i$ ( $\text{mm y}^{-1}$ )	$0.085 \pm 0.003$	$0.081 \pm 0.003$	$0.076 \pm 0.003$	$0.071 \pm 0.003$	$0.090 \pm 0.003$	$0.094 \pm 0.003$

the HRTEM images of Areas A and B in Fig. 6a, respectively. It can be seen from Area C in Fig. 6b that when the alloy was impacted by  $\text{Al}_2\text{O}_3$  particles, through the effects of force, the arrangement of atoms in this area became relatively disordered, and a banded area with a weakened lattice appeared. The disordered arrangement belonged to the high-energy dislocation region, which was conducive to local lattice torsion, which may develop further into dislocation walls or subgrain boundaries [23, 24]. It can be seen from Areas D and E in Fig. 6c that there are high-density dislocation arrays and dislocation entanglements in different orientations in these two regions. In the deformation process, this area was subjected to concentrated stress, forming deformation twins and substructures, taking advantage of the deformation.

It can be seen from Fig. 6d that there are nanocrystalline grains in Area F. Figure 6e is an enlarged image of Area F in Fig. 6d. The nanocrystalline grain boundary (Area G) and center (Area H) are enlarged, as shown in Fig. 6f, where Area I corresponds to Area G in Fig. 6e. In Area I, the nanocrystalline grain boundary area has no clear boundaries, but there are a large number of dislocation slips in the fuzzy area. Area J corresponds to Area H in Fig. 6e. As can be seen from the figure, Area J has a large number of striped stress-derivative images in the central area of the nanocrystalline grains, indicating that there is still stress concentrated in the newly formed nanocrystalline grains in the deformation layer. This provided the deformation driving force for the subsequent segmentation and refinement of the grains.

It can be seen from Figs. 5, 6 that at  $35 \mu\text{m}$  below the surface of the  $E_{30}$  alloy, there are micro-deformed micron grains, dislocations, nanocrystals, and striped substructures in the deformed region, indicating that the layer is still in a state of continuous refinement.

### 3.2. Mechanical properties

The mechanical properties of the as-extruded Mg-1.8Zn-0.5Zr-1.5Gd alloy subjected to SFPB for different times are shown in Fig. 7. As the bombardment time increased from 0 to 50 s, the mechanical properties of the alloy first increased and then decreased. When the bombardment time was 30 s, the alloy had better mechanical properties, and its tensile strength, YS, and EL were  $299.1 \pm 2.2 \text{ MPa}$ ,  $264.4 \pm 1.5 \text{ MPa}$ , and  $36.8 \pm 1.3 \%$ , respectively.

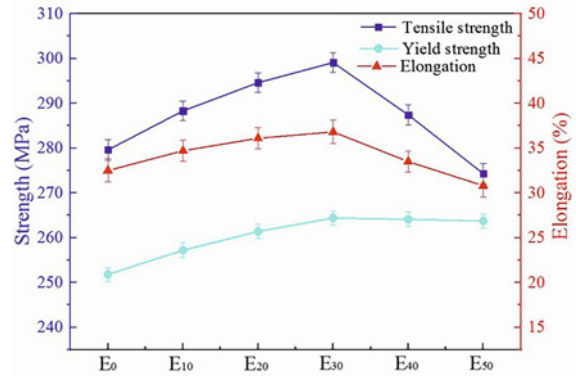


Fig. 7. Tensile properties of the Mg-1.8Zn-0.5Zr-1.5Gd alloy subjected to SFPB.

The tensile fracture morphologies of the as-extruded Mg-1.8Zn-0.5Zr-1.5Gd alloys subjected to SFPB for different times are shown in Fig. 8. It can be seen from Fig. 8 that the tensile fractures of all samples were mainly composed of torn edges, dimples, and cleavage planes. The proportion of these three changed with an increase in the bombardment time. At the same time, they all showed obvious features of ductile fractures. It can be seen from Figs. 8a–d that with the prolongation of the bombardment time, the proportion of dimples increased gradually, and the size of the dimples also increased significantly. When the bombardment time was 30 s, uniform and equiaxed dimples were distributed throughout the fracture, and the corresponding mechanical properties also reached the maximum value. With a further extension of the bombardment time, the proportion and size of the cleavage planes in the fracture gradually increased, while the proportion and size of dimples gradually decreased, and the corresponding mechanical properties gradually decreased.

### 3.3. Corrosion resistance

Figure 9 shows the polarization curves of the alloys after immersion in SBF for 1 h (Fig. 9a) and  $\nu_w$  and  $\nu_H$  in the alloys after 120 h of immersion (Fig. 9b). Table 1 shows the self-corrosion potential ( $E_{\text{corr}}$ ), self-corrosion current density ( $I_{\text{corr}}$ ), and self-corrosion rate ( $P_i$ ) obtained from Fig. 9a by Tafel extrapolating. As can be seen from Fig. 9 and Table 1, when the bombardment time was less than 30 s, with an increase in the bombardment time,  $E_{\text{corr}}$  gradu-

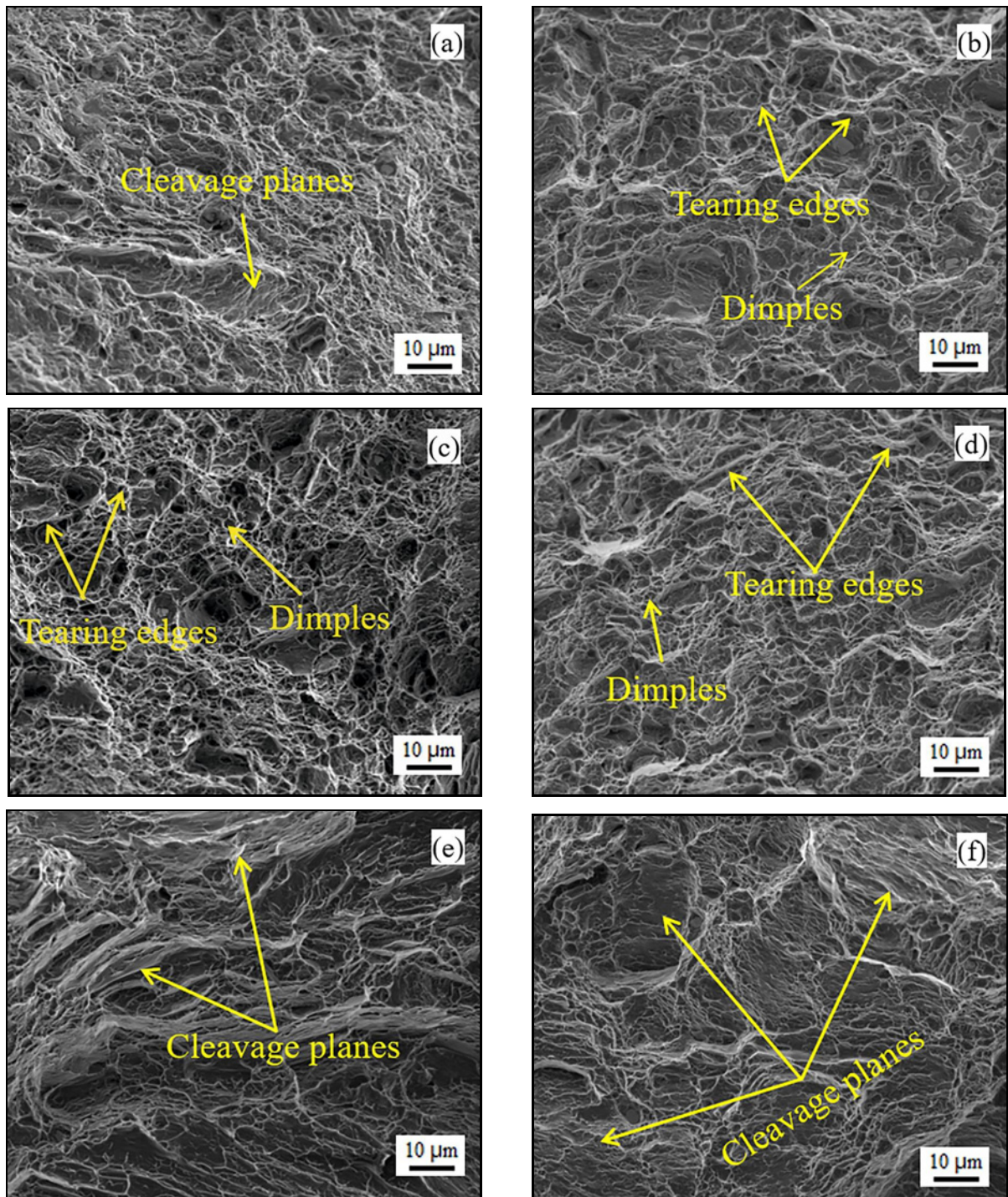


Fig. 8. Tensile fracture morphology of Mg-1.8Zn-0.5Zr-1.5Gd alloys subjected to SFPB: (a)  $E_0$ , (b)  $E_{10}$ , (c)  $E_{20}$ , (d)  $E_{30}$ , (e)  $E_{40}$ , and (f)  $E_{50}$ .

ally moved in the positive direction,  $I_{\text{corr}}$ ,  $P_1$ ,  $\nu_w$ , and  $\nu_H$  decreased gradually, and the corrosion resistance gradually increased. When the bombardment time was greater than 30 s,  $E_{\text{corr}}$  gradually moved in the negative direction with an increase in the bombardment time;  $I_{\text{corr}}$ ,  $P_1$ ,  $\nu_w$ , and  $\nu_H$  gradually increased, and the corrosion resistance gradually weakened. When the bombardment time was 30 s, the alloy had bet-

ter corrosion resistance.

Figure 10 and Table 2 show the corrosion morphologies and the results of the EDS analysis for alloys immersed in SBF for 120 h after being subjected to SFPB at different times. It can be seen from Fig. 10 that the corrosion products on the alloy's surface were mainly composed of dense gray corrosion products and loose white corrosion products. As shown in Fig. 10d,

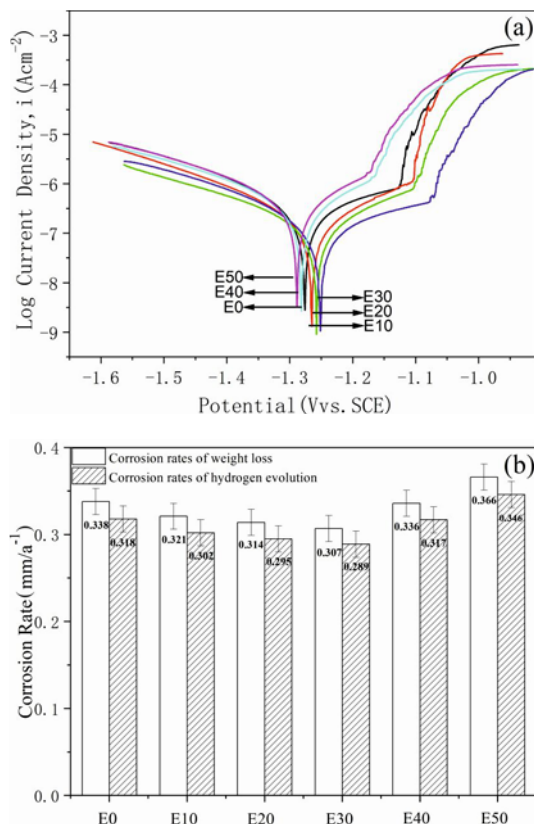


Fig. 9. Polarization curves for alloys subjected to SFPB after immersion in SBF for 1 h, and  $\nu_w$  and  $\nu_H$  after immersion in SBF for 120 h.

Table 2. EDS analyses of the  $E_{30}$  alloy after immersion in SBF for 120 h

Position	Mass fraction (%)				
	C	O	Mg	P	Ca
A	16.24	37.89	4.07	17.73	24.07
B	16.47	37.95	9.21	16.58	19.78

EDS analysis was performed on the dense black corrosion products (Area A) and the loose white corrosion products (Area B) in the  $E_{30}$  alloy's corrosion layer. As shown in Table 2, the corrosion products in Areas A and B are mainly composed of the elements C, O, Mg, P, and Ca, and the corrosion products in Areas A and B only have different proportions of these different elements. At the same time, it can be seen that the elements in the corrosion layer are also the main elements of  $\text{Ca}_{10}(\text{PO}_4)_6(\text{OH})_2$ .  $\text{Ca}_{10}(\text{PO}_4)_6(\text{OH})_2$  can induce the formation and growth of new bone tissue and is often used as a modification material for biological surfaces [25, 26].

It can also be seen from Figs. 10e,f that there

are local raised areas in the corrosion layer, and the raised areas also have wide cracks caused by moisture loss in the corrosion layer. This indicates that the degradation rate in this local area was high during the degradation process and that pitting corrosion occurred [27].

Figure 11 shows the corrosion morphology of the alloy's surface after removing the corrosion products. It can be seen from Fig. 11a that the morphology of the  $E_0$  alloy after corrosion was relatively uniform, but a very small amount of corrosion pores with a size of about  $3\ \mu\text{m}$  can be seen on the surface. The appearance of the corrosion pores can be considered to be caused by the nanoscale second-phase particles (Fig. 3) in the alloy matrix, which act as cathodes during the corrosion process, accelerating the corrosion of the surrounding alloy matrix. The rapid corrosion of the matrix around the nanoscale second-phase particles and their own shedding result in a small amount of corrosion pores on the surface of the alloy after corrosion [28]. When the bombardment time was 0–30 s, as shown in Figs. 11b–d, with an increase in the SFPB treatment time, the number and size of the corrosion holes on the surface of the alloy after corrosion gradually increased. The surface roughness of the alloy (Fig. 2) increased slowly with an increase in the bombardment time. It can be inferred that the degree of deformation, and the size and number of microcracks in the local area of the alloy's surface will also gradually increase. The faster corrosion rate in the local area produced more serious deformation and microcracks, leading to corrosion holes in this area [29]. As a result, after the alloy corroded, the number and size of the surface corrosion holes gradually increased with increased bombardment time. When the bombardment time was 40–50 s, as shown in Figs. 11e,f, the number and size of the corrosion holes on the surface of the alloy after corrosion increased rapidly with an increase in the bombardment time. At the same time, Areas A and B in Figs. 10e,f were enlarged, it was seen that the corrosion holes (Area A) developed from an isolated distribution state to a state of a mutual contact or a merger (Area B), and the diameter of the larger corrosion holes reached about  $20\ \mu\text{m}$ . When the bombardment time reached 40 s, the surface roughness of the alloy increased rapidly to  $8.207\ \mu\text{m}$ ; at the same time, the size of the microcracks on the alloy's surface (Fig. 1) also increased rapidly. The increase in the roughness indicated the increase in the degree of local deformation, which will also produce more high-density dislocation regions. During the corrosion process, the areas with local high-density dislocation and microcracks regions that have poor thermal stability will act as anodes to accelerate their own corrosion and generate more large-sized corrosion pores [30]. When the bombardment time increased to 50 s, the surface roughness of the alloy in-

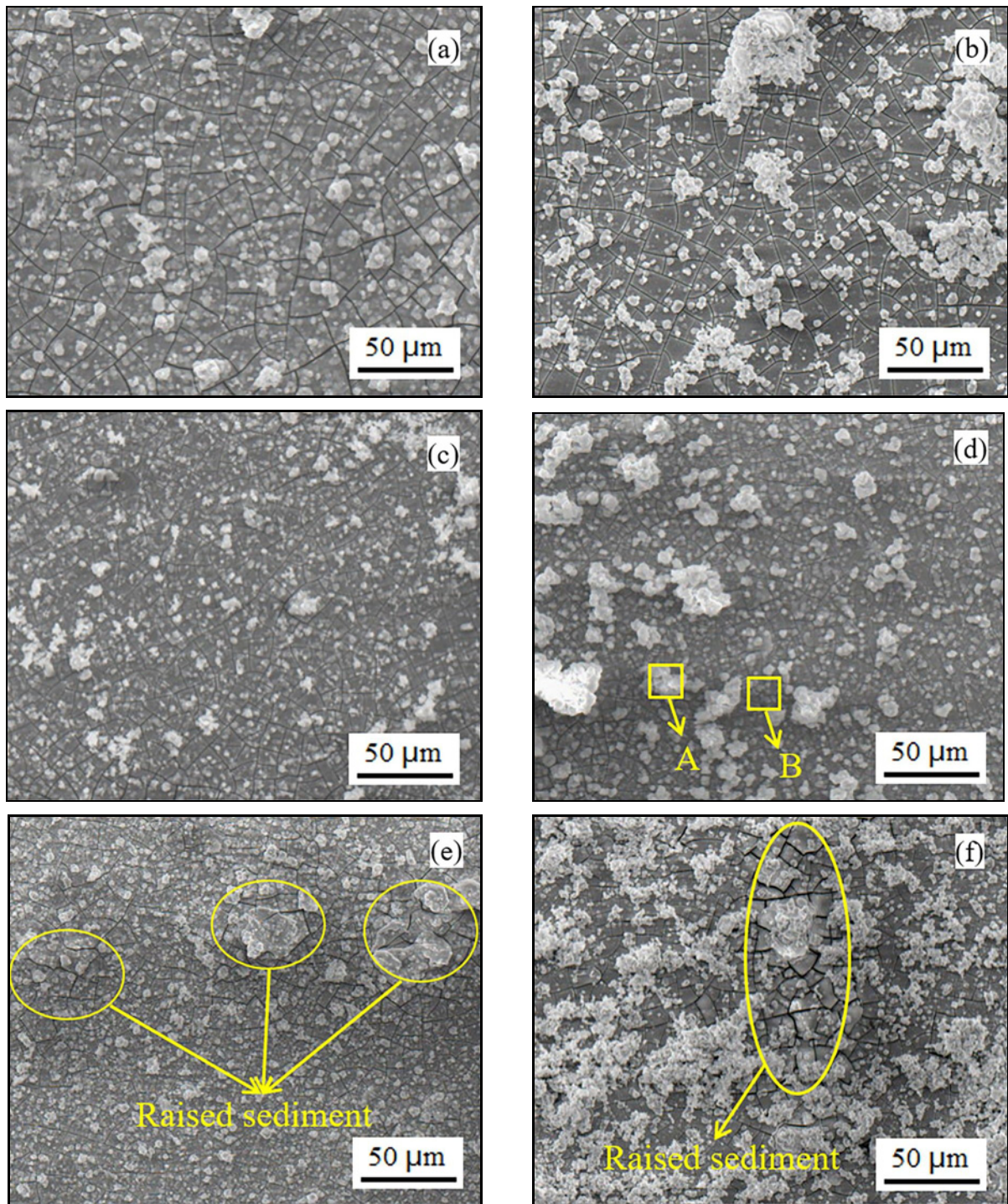


Fig. 10. SEM morphology and EDS analysis of a Mg-1.8Zn-0.5Zr-1.5Gd alloy subjected to SFPB then immersed in SBF for 120 h: (a)  $E_0$ , (b)  $E_{10}$ , (c)  $E_{20}$ , (d)  $E_{30}$ , (e)  $E_{40}$ , and (f)  $E_{50}$ .

creased further, resulting in a further increase in local high-density dislocation regions and microcrack regions. During the corrosion process, more corrosion holes were generated, and, at the same time, the expansion and merger of corrosion holes also occurred, forming a larger corrosion hole, as shown in Area B in Fig. 11f.

Figure 12 shows the average degradation rate ( $\nu_w$ ) of the  $E_{30}$  alloy every 8 h after immersion in SBF for 120 h. The  $\nu_w$  of the alloy gradually decreased with an increase in the immersion time within the first 24 h, then the  $\nu_w$  of the alloy gradually increased with an increase in the immersion time from 24 to 64 h. The  $\nu_w$  then decreased gradually with an increase in the

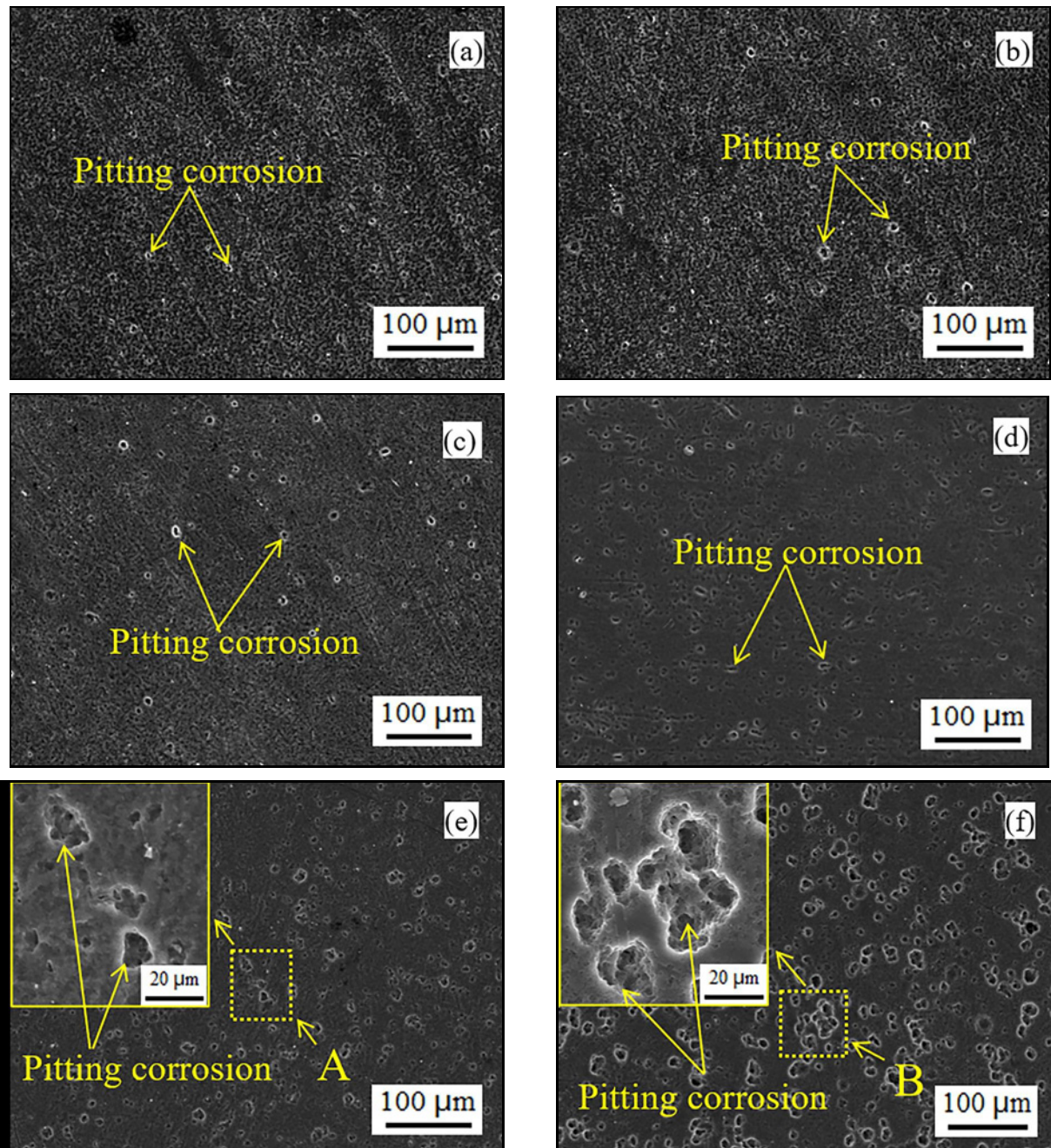


Fig. 11. SEM images of the morphology of a Mg-1.8Zn-0.5Zr-1.5Gd alloy subjected to SFPB and immersed in SBF for 120 h after removing the corrosion products: (a)  $E_0$ , (b)  $E_{10}$ , (c)  $E_{20}$ , (d)  $E_{30}$ , (e)  $E_{40}$ , and (f)  $E_{50}$ .

immersion time from 64 to 104 h, finally reaching a plateau after 104 h.

#### 4. Discussion

According to the Hall-Petch equation [31], grain refinement is one of the main means used to improve the mechanical properties of magnesium alloys. Through grain refinement, the density of grain boundary per unit of volume in the alloy can be increased, and the

resistance of the dislocation network that needs to be overcome during the movement of dislocations can be increased. In addition, grain refinement can also shorten the length of the accumulated dislocations per unit of volume in the alloy and makes it harder to concentrate the stress. It requires a large external force to activate dislocations in the adjacent grains, which usually means that the strength of the alloy increases with a decrease in the grain size [32]. Therefore, the  $E_0$  alloy with a fine grain size had higher mechanical properties. In extruded magnesium alloys with fine

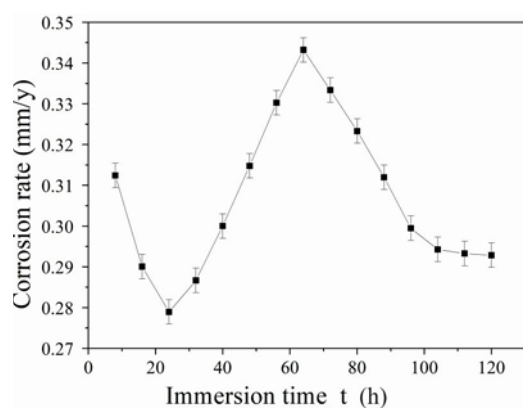


Fig. 12. Average  $\nu_w$  corrosion rates for the  $E_{30}$  alloy as measured by weight loss every 8 h.

grains, the internal microstructure will gradually separate and form microscopic voids through the action of tensile stress. At the same time, the number and size of the microscopic voids will also gradually increase under the action of slippage. When many voids begin to aggregate and connect with each other, they will lead to fractures, forming a dimple-like fracture morphology with ductile fracture properties [33, 34]. Therefore, as shown in Fig. 7a, the tensile fractures of the  $E_0$  alloy were mainly composed of uniform and equiaxed dimples and a very small amount of quasi-cleavage planes, showing typical characteristics of ductile fractures.

When the bombardment time was between 10 and 30 s, with an increase in the bombardment time, as shown in Figs. 1b–d, the surface grains of the alloy were refined to a certain extent under the bombardment of high-energy particles. The depth of grain refinement from the surface layer to the core increased further. This grain refinement can improve the strength of the alloy; at the same time, it can also prevent the concentration of stress and improve the alloy's ductility [35]. After the alloy has been subjected to SFPB, a residual compressive stress field will be formed on the surface of the alloy, and its strength will increase with an increase in the bombardment time. During the process of stretching the material, the residual compressive stress on the surface of the material can balance part of the tensile stress during the process of the material bearing the tensile stress, so that the actual tensile stress suffered by the material is reduced, which is beneficial for reducing the speed of crack initiation and expansion, thus improving the strength and elongation of the material [36]. Therefore, with an increase in the bombardment time, the mechanical properties and elongation of the alloy gradually increased. From a macroscopic point of view, the increase in elongation will lead to an increase in the size of microscopic voids formed during the

stretching process. Therefore, as shown in Figs. 7b–d, the size and depth of the dimples in the fractures of the alloy increased the time of bombardment.

When the bombardment time was greater than 30 s, as shown in Fig. 2, the surface roughness of the alloy increased further with an increase in the bombardment time. At the same time, as shown in Fig. 1, a certain number of microcracks also appeared on the surface of the alloy, and the size of the microcracks gradually increased with an increase in the bombardment time. During the stretching process, the stress concentration phenomenon generated at the tip of the microcrack caused the actual stress in the microcrack to be much higher than the apparent stress [37], causing the microcrack to become a channel for crack propagation and causing the instability to extend. The extended instability led to a fracturing of the alloy and a decrease in the tensile strength. Therefore, the strength and elongation of the alloy gradually decreased with an increase in the bombardment time. At the same time, because of the severe plastic deformation on the surface of the alloy, the significant increase in the dislocation density and the increase in the size of microcracks, the plasticity of the surface layer of the alloy reduced, and a large area of cleavage surfaces was generated in the tensile fracture morphology. The fracture mode was characterized by a mixture of ductile and brittle fractures. Therefore, as shown in Figs. 7e,f, the proportion of cleavage planes in the fractures of the alloy increased with an increase in the bombardment time.

SFPB can form a nanocrystalline layer on the surface of the extruded Mg-1.8Zn-0.5Zr-1.5Gd alloy. The nanocrystalline structure usually has high surface activity and a high specific surface area. In an inert SBF solution, the nanocrystalline structure can promote the passivation effect of the alloy surface, preventing the progress of corrosion and improving the corrosion resistance of the alloy [38]. Mg and MgO have different crystal structures. The larger the grain size of the alloy, the easier it is to cause a discontinuity in the two-phase interface between the matrix Mg and the surface MgO film. Nanometering the surface of the magnesium alloy can reduce the difference between the matrix Mg and the surface MgO film. The discontinuity of the phase interface reduces the tensile stress or compressive stress between the interfaces and reduces the tendency of the MgO film to rupture [39]. During the SFPB process, a dense MgO film will be formed on the surface of the nanocrystalline layer. During the corrosion process, the dense MgO film can better protect the substrate Mg; at the same time, the dense MgO film can reduce the surface  $Mg(OH)_2$  layer, which is prone to cracking, and improve the corrosion resistance of the alloy [40]. After SFPB, the density of the alloy surface structure is improved, which can eliminate the adverse effects of microscopic pores and

other defects on the corrosion resistance and enhance the corrosion resistance of the alloy's surface [41, 42]. During the corrosion process of magnesium alloys, the corrosion products will generate a certain amount of tensile stress on the surface of the alloy. After SFPB, the residual compressive stress on the surface of the alloy can offset part of the tensile stress and reduce the cracking tendency of the MgO film on the surface of the alloy, thereby enhancing the stability and anti-corrosion protective effects of MgO films [43]. When the bombardment time was 0–30 s, the thickness of the nanocrystalline layer on the surface of the alloy, the density of the surface layer structure, and the surface residual compressive stress, all increased with an increase in the bombardment time. Therefore, the corrosion resistance of the alloy increased with the bombardment time.

When the bombardment time was longer than 30 s, larger cracks began to appear on the surface of the alloy. Therefore, the size and number of cracks on the surface of the alloy played a leading role in the corrosion resistance of the alloy. There was a large difference in the grain size and dislocation density between the crack tip area on the surface of the alloy and the bottom area of the adjacent crack. During the corrosion process, galvanic corrosion of the crack tip area and the bottom area of the adjacent crack formed, which will accelerate the alloy's corrosion. At the same time, an increase in the cracks' size also led to an increase in the contact area between the SBF solution and the alloy, which also accelerated the corrosion of the alloy. When the bombardment time was greater than 30 s, the size and number of the surface cracks in the alloy increased rapidly with an increase in the bombardment time. Therefore, the corrosion resistance of the alloy gradually decreased with an increase in the bombardment time.

According to the changes in the  $\nu_w$  of the  $E_{30}$  alloy within 120 h of immersion in SBF, the corrosion process of the alloy could be divided into four stages: In the first stage (0–24 h), it can be considered that in the first 8 h of immersion, the surface of the alloy was completely exposed to the SBF solution and the alloy had a high corrosion rate; at the same time, a layer of loose  $\text{Mg}(\text{OH})_2$  corrosion products rapidly formed on the surface of the alloy [44]. With a further increase in the immersion time, the increased amount of  $\text{Mg}(\text{OH})_2$  corrosion products on the alloy surface reduced the effective contact area between the alloy matrix and the SBF solution and hindered the progress of the reaction. Therefore, the corrosion rate of the alloy decreases with an increase in immersion time. At the same time, the nanocrystals on the surface of the alloy were continuously dissolved by the progress of the corrosion reaction, and their thickness was reduced continuously. In the second stage (24–64 h), the alloy's area of surface roughness and the microcrack

area had a higher corrosion rate. Therefore, as the corrosion reaction continued, the areas with larger roughness and microcracks were the first to expose large grains unaffected by SFPB. There was a difference in the thermodynamic stability between the exposed large grains and their adjacent nanograins. During the corrosion process, the large grains and the surrounding nanograins will form a galvanic cell and accelerate the dissolution of the large grains, which act as the anodes. As a result, the corrosion rate gradually increased with an increase in the immersion time [45]. The corrosion rate of Mg alloys in the SBF solution with a passivation environment increased with an increase in grain size [46]. Therefore, within 24–64 h, the corrosion rate of the alloy gradually increased with an increase in the immersion time. In the third stage (64–104 h), with the continuation of the corrosion reaction, the thickness of the loose  $\text{Mg}(\text{OH})_2$  corrosion layer on the surface of the alloy continued to increase. There were also higher concentrations of free  $\text{Mg}^{2+}$  in the adjacent region. Inside the  $\text{Mg}(\text{OH})_2$  corrosion layer and the adjacent areas, the higher concentration of  $\text{Mg}^{2+}$  will react with the  $\text{Ca}^{2+}$ ,  $\text{H}_2\text{PO}_4^{4-}$  and  $\text{HPO}_4^{2-}$  in the solution to generate  $(\text{Ca},\text{Mg})_3(\text{PO}_4)_2$  and  $\text{Ca}_{10}(\text{PO}_4)_6(\text{OH})_2$  corrosion products, and continuously consume the  $\text{Mg}(\text{OH})_2$  corrosion products in the corrosion layer. With an increase in the immersion time, the corrosion layer gradually changed from the initial loose  $\text{Mg}(\text{OH})_2$  corrosion products to a combination of dense  $\text{Mg}(\text{OH})_2$ ,  $(\text{Ca},\text{Mg})_3(\text{PO}_4)_2$  and  $\text{Ca}_{10}(\text{PO}_4)_6(\text{OH})_2$  corrosion products [47]. Within 64–104 h, the thickness of the dense corrosion products increased with an increase in the immersion time, and the thickening of the dense corrosion products hindered the progress of the corrosion reaction. Therefore, the corrosion rate of the alloy at this stage decreased continuously with an increase in the immersion time. In the fourth stage (104–120 h), the formation and dissolution of corrosion products on the surface of the alloy during the immersion process in SBF was a dynamic process [48]. It can be considered that when the immersion time was longer than 104 h, the formation and dissolution of corrosion products on the surface of the alloy reached a dynamic equilibrium during the renewal process of SBF every 8 h, so the corrosion rate of the alloy gradually tended to become stable.

These experimental results show that the thickness of the nanocrystalline layer on the surface of the medical magnesium alloy can be adjusted by changing the bombardment time; in other words, the change law of its corrosion rate in SBF can be adjusted. It meets the requirements of medical magnesium alloy implant materials of having a low corrosion rate in the early stage and ensures that it can provide sufficient strength to function as a fixed support for a long period of time. In addition, as an implant material, a magnesium alloy must have a high corrosion rate

in the later period of retention in the human body, so that its strength will decrease rapidly, thus transferring more load to the new bone tissue, and finally achieving complete degradation.

## 5. Conclusions

1. SFPB can be used to form a nanostructure with a certain depth gradient on the surface of a magnesium alloy, and its depth and surface roughness increase with an increase in the bombardment time. When the bombardment time is 30 s, microcracks begin to appear on the alloy's surface; with the prolongation of the bombardment time, the number of microcracks gradually increases, and their depth also increases significantly.

2. When the bombardment time is between 0 and 30 s, the thickness of the nanocrystalline layer on the surface of the alloy increases with an increase in the bombardment time, which leads to the gradual enhancement of the mechanical properties of the alloy with an increase in the bombardment time. When the bombardment time was between 30 and 50 s, the size of the microcracks that are prone to stress concentrations increases with an increase in the bombardment time, resulting in a continuous decrease in the mechanical properties of the alloy.

3. When the bombardment time is between 0 and 30 s, with an increase in the bombardment time, the thickness of the nanocrystalline layer that promotes the passivation effect on the surface of the alloy gradually increases, and the corrosion resistance of the alloy gradually increases. When the bombardment time is 30–50 s, the galvanic corrosion of the microcrack tip area on the surface of the alloy and its adjacent areas accelerates the corrosion of the alloy, and the corrosion resistance of the alloy gradually decreases. During immersion of the  $E_{30}$  alloy for 120 h, the corrosion rate of the alloy first decreases, then increases, and then decreases with an increase in the immersion time, and finally tends to become stable.

## Acknowledgements

This work was supported by the Education Department of Henan Province (20A430010), the National Natural Science Foundation of China (U1804146), and the Academy of Finland (profile grant No. 311934).

## References

- [1] M. I. Jamesh, G. Wu, Y. Zhao, W. Jin, D. R. McKenzie, M. M. M. Bilek, P. K. Chu, Effects of zirconium and nitrogen plasma immersion ion implantation on the electrochemical corrosion behavior of Mg-Y-RE alloy in simulated body fluid and cell culture medium, *Corros. Sci.* 86 (2014) 239–251. <https://doi.org/10.1016/j.corsci.2014.05.020>
- [2] D. Liu, S. Hu, X. Yin, J. Liu, Z. Jia, Q. Li, Degradation mechanism of magnesium alloy stent under simulated human micro-stress environment, *Mater. Sci. Eng. C* 84 (2018) 263–270. <https://doi.org/10.1016/j.msec.2017.12.001>
- [3] X. Guo, G. Liu, S. Sang, Q. Lin, Y. Qiao, Characteristics and surface serviceability for cryogenic milling Mg-1.6Ca-2.0Zn medical magnesium alloy, *J. Funct. Biomater.* 13 (2022) 179. <https://doi.org/10.3390/jfb13040179>
- [4] D. B. Prabhu, J. Nampoothiri, V. Elakkiya, R. Narmadha, R. Selvakumar, R. Sivasubramanian, P. Gopalakrishnan, K. R. Ravi, Elucidating the role of microstructural modification on stress corrosion cracking of biodegradable Mg<sub>4</sub>Zn alloy in simulated body fluid, *Mater. Sci. Eng. C* 106 (2020) 110164. <https://doi.org/10.1016/j.msec.2019.110164>
- [5] E. K. Brooks, S. Der, M. T. Ehrensberger, Corrosion and mechanical performance of AZ91 exposed to simulated inflammatory conditions, *Mater. Sci. Eng. C* 60 (2016) 427–436. <https://doi.org/10.1016/j.msec.2015.11.059>
- [6] Y. Chen, Z. Xu, C. Smith, J. Sankar, Recent advances on the development of magnesium alloys for biodegradable implants, *Acta Biomater.* 10 (2014) 4561–4573. <https://doi.org/10.1016/j.actbio.2014.07.005>
- [7] L. Choudhary, R. K. S. Raman, Mechanical integrity of magnesium alloys in a physiological environment: Slow strain rate testing based study, *Eng. Fract. Mech.* 103 (2013) 94–102. <https://doi.org/10.1016/j.engfracmech.2012.09.016>
- [8] W. T. Huo, W. Zhang, J. W. Lu, Y. S. Zhang, Simultaneously enhanced strength and corrosion resistance of Mg-3Al-1Zn alloy sheets with nano-grained surface layer produced by sliding friction treatment, *J. Alloys Compd.* 720 (2017) 324–331. <https://doi.org/10.1016/j.jallcom.2017.05.258>
- [9] J. Li, L. Tan, P. Wan, X. Yu, K. Yang, Study on microstructure and properties of extruded Mg-2Nd-0.2Zn alloy as potential biodegradable implant material, *Mater. Sci. Eng. C* 49 (2015) 422–429. <https://doi.org/10.1016/j.msec.2015.01.029>
- [10] H. Yao, J. Wen, Y. Xiong, Y. Lu, F. Ren, W. Cao, Extrusion temperature impacts on biometallic Mg-2.0Zn-0.5Zr-3.0Gd (wt%) solid-solution alloy, *J. Alloys Compd.* 739 (2018) 468–480. <https://doi.org/10.1016/j.jallcom.2017.12.225>
- [11] X. Zhang, Z. Ba, Z. Wang, Y. Wu, Y. Xue, Effect of LPSO structure on mechanical properties and corrosion behavior of as-extruded GZ51K magnesium alloy, *Mater. Lett.* 163 (2016) 250–253. <https://doi.org/10.1016/j.matlet.2015.10.084>
- [12] S. Wu, S. Wang, G. Wang, X. Yu, W. Liu, Z. Chang, D. Wen, Microstructure, mechanical and corrosion properties of magnesium alloy bone plate treated by high-energy shot peening, *Trans. Nonferrous Met. Soc. China* 29 (2019) 1641–1652. [https://doi.org/10.1016/S1003-6326\(19\)65071-5](https://doi.org/10.1016/S1003-6326(19)65071-5)
- [13] C. Liu, H. Zheng, X. Gu, B. Jiang, J. Liang, Effect of severe shot peening on corrosion behavior of AZ31 and AZ91 magnesium alloys, *J. Alloys Compd.* 770 (2019)

- 500–506.  
<https://doi.org/10.1016/j.jallcom.2018.08.141>
- [14] G. Y. Yuan, J. L. Niu, Research progress of biodegradable magnesium alloys for orthopedic applications, *Acta Met. Sin.* 53 (2017) 1168–1180.  
<https://doi.org/10.11900/0412.1961.2017.00247>
- [15] H. Yao, J. B. Wen, Y. Xiong, Y. Lu, M. Huttula, Microstructure evolution in Mg-Zn-Zr-Gd biodegradable alloy: The decisive bridge between extrusion temperature and performance, *Front. Chem.* 6 (2018) 71.  
<https://doi.org/10.3389/fchem.2018.00071>
- [16] Z. Shi, M. Liu, A. Atrens, Measurement of the corrosion rate of magnesium alloys using Tafel extrapolation, *Corros. Sci.* 52 (2010) 579–588.  
<https://doi.org/10.1016/j.corsci.2009.10.016>
- [17] N. I. Z. Abidin, A. D. Atrens, D. Martin, A. Atrens, Corrosion of high purity Mg, Mg2Zn0.2Mn, ZE41 and AZ91 in Hank's solution at 37°C, *Corros. Sci.* 53 (2011) 3542–3556.  
<https://doi.org/10.1016/j.corsci.2011.06.030>
- [18] L. Zhang, A. Ma, J. Jiang, D. Song, D. Yang, J. Chen, Electrochemical corrosion properties of the surface layer produced by supersonic fine-particles bombarding on low-carbon steel, *Surf. Coat. Technol.* 232 (2013) 412–418.  
<https://doi.org/10.1016/j.surfcoat.2013.05.043>
- [19] H. Yao, B. Fang, H. Shi, H. Singh, M. Huttula, W. Cao, Microstructures, mechanical properties and degradation behavior of as-extruded Mg-1.8Zn-0.5Zr-xGd ( $0 \leq x \leq 2.5$  wt.%) biodegradable alloys, *J. Mater. Sci.* 56 (2021) 11137–11153.  
<https://doi.org/10.1007/s10853-021-05982-3>
- [20] K. Xu, A. Wang, Y. Wang, X. Dong, X. Zhang, Z. Huang, Surface nanocrystallization mechanism of a rare earth magnesium alloy induced by HVOF supersonic microparticles bombarding, *Appl. Surf. Sci.* 256 (2009) 619–626.  
<https://doi.org/10.1016/j.apsusc.2009.06.098>
- [21] T. Zhou, Y. Xiong, Z. Chen, X. Zha, Y. Lu, T. He, F. Ren, H. Singh, J. Kömi, M. Huttula, W. Cao, Effect of surface nano-crystallization induced by supersonic fine particles bombarding on microstructure and mechanical properties of 300M steel, *Surf. Coat. Technol.* 421 (2021) 127381.  
<https://doi.org/10.1016/j.surfcoat.2021.127381>
- [22] R. Zhang, X. Zhou, H. Gao, S. Mankoci, Y. Liu, X. Sang, H. Qin, X. Hou, Z. Ren, G. L. Doll, A. Martini, Y. Dong, N. Sahai, C. Ye, The effects of laser shock peening on the mechanical properties and biomedical behavior of AZ31B magnesium alloy, *Surf. Coat. Technol.* 339 (2018) 48–56.  
<https://doi.org/10.1016/j.surfcoat.2018.02.009>
- [23] M. S. Wu, Analysis of dislocation wall formation in a disclinated nanograin, *Int. J. Plast.* 26 (2010) 794–805.  
<https://doi.org/10.1016/j.iijplas.2009.10.007>
- [24] E. A. Rzhavtsev, M. Y. Gutkin, The dynamics of dislocation wall generation in metals and alloys under shock loading, *Scr. Mater.* 100 (2015) 102–105.  
<https://doi.org/10.1016/j.scriptamat.2015.01.004>
- [25] P. J. Burke, Z. Bayindir, G. J. Kipouros, X-ray photoelectron spectroscopy (XPS) investigation of the surface film on magnesium powders, *Appl. Spectrosc.* 66 (2012) 540–518. <https://doi.org/10.1366/11-06372>
- [26] X. Lin, X. Wang, L. Tan, P. Wan, X. Yu, Q. Li, K. Yang, Effect of preparation parameters on the properties of hydroxyapatite containing microarc oxidation coating on biodegradable ZK60 magnesium alloy, *Ceram. Int.* 40 (2014) 10043–10051.  
<https://doi.org/10.1016/j.ceramint.2014.02.104>
- [27] W. Ma, Y. Liu, W. Wang, Y. Zhang, Effects of electrolyte component in simulated body fluid on the corrosion behavior and mechanical integrity of magnesium, *Corros. Sci.* 98 (2015) 201–210.  
<https://doi.org/10.1016/j.corsci.2015.05.012>
- [28] F. Cao, K. Deng, K. Nie, J. Kang, H. Niu, Microstructure and corrosion properties of Mg-4Zn-2Gd-0.5Ca alloy influenced by multidirectional forging, *J. Alloys Compd.* 770 (2019) 1208–1220.  
<https://doi.org/10.1016/j.jallcom.2018.08.191>
- [29] S. Bagherifard, D. J. Hickey, S. Fintová, F. Pastorek, I. Fernandez-Pariente, M. Bandini, T. J. Webster, M. Guagliano, Effects of nanofeatures induced by severe shot peening (SSP) on mechanical, corrosion and cytocompatibility properties of magnesium alloy AZ31, *Acta Biomater.* 66 (2018) 93–108.  
<https://doi.org/10.1016/j.actbio.2017.11.032>
- [30] H. Y. Choi, W. J. Kim, Effect of thermal treatment on the bio-corrosion and mechanical properties of ultrafine-grained ZK60 magnesium alloy, *J. Mech. Behav. Biomed. Mater.* 51 (2015) 291–301.  
<https://doi.org/10.1016/j.jmbbm.2015.07.019>
- [31] D. K. Xu, L. Liu, Y. B. Xu, E. H. Han, The influence of element Y on the mechanical properties of the as-extruded Mg-Zn-Y-Zr alloys, *J. Alloys Compd.* 426 (2006) 155–161.  
<https://doi.org/10.1016/j.jallcom.2006.02.035>
- [32] M. Mabuchi, K. Kubota, K. Higashi, New recycling process by extrusion for machined chips of AZ91 magnesium and mechanical properties of extruded bars, *Mater. Trans., JIM* 36 (1995) 1249–1254.  
<https://doi.org/10.2320/matertrans1989.36.1249>
- [33] X. Pan, G. Qian, Y. Hong, Nanograin formation in dimple ridges due to local severe-plastic-deformation during ductile fracture, *Scr. Mater.* 194 (2021) 113631.  
<https://doi.org/10.1016/j.scriptamat.2020.113631>
- [34] H. Miao, H. Huang, Y. Shi, H. Zhang, J. Pei, G. Yuan, Effects of solution treatment before extrusion on the microstructure, mechanical properties and corrosion of Mg-Zn-Gd alloy in vitro, *Corros. Sci.* 122 (2017) 90–99. <https://doi.org/10.1016/j.corsci.2017.01.001>
- [35] D. K. Xu, L. Liu, Y. B. Xu, E. H. Han, The influence of element Y on the mechanical properties of the as-extruded Mg-Zn-Y-Zr alloys, *J. Alloys Compd.* 426 (2006) 155–161.  
<https://doi.org/10.1016/j.jallcom.2006.02.035>
- [36] J. Zhao, Y. Dong, C. Ye, Laser shock peening induced residual stresses and the effect on crack propagation behavior, *Int. J. Fatigue* 100 (2017) 407–417.  
<https://doi.org/10.1016/j.ijfatigue.2017.04.002>
- [37] S. Y. Lee, P. K. Liaw, H. Choo, R. B. Rogge, A study on fatigue crack growth behavior subjected to a single tensile overload: Part I. An overload-induced transient crack growth micromechanism, *Acta Mater.* 59 (2011) 485–494.  
<https://doi.org/10.1016/j.actamat.2010.09.049>
- [38] B. R. Sunil, T. S. S. Kumar, U. Chakkingal, V. Nandakumar, M. Doble, V. D. Prasad, M. Raghunath, In vitro and in vivo studies of biodegradable fine grained

- AZ31 magnesium alloy produced by equal channel angular pressing, *Mater. Sci. Eng. C* 59 (2016) 356–367. <https://doi.org/10.1016/j.msec.2015.10.028>
- [39] G. R. Argade, S. K. Panigrahi, R. S. Mishra, Effects of grain size on the corrosion resistance of wrought magnesium alloys containing neodymium, *Corros. Sci.* 58 (2012) 145–151. <https://doi.org/10.1016/j.corsci.2012.01.021>
- [40] J. Liao, M. Hotta, N. Yamamoto, Corrosion behavior of fine-grained AZ31B magnesium alloy, *Corros. Sci.* 61 (2012) 208–214. <https://doi.org/10.1016/j.corsci.2012.04.039>
- [41] V. K. Caralapatti, S. Narayanswamy, Effect of high repetition laser shock peening on biocompatibility and corrosion resistance of magnesium, *Opt. Laser Technol.* 88 (2017) 75–84. <https://doi.org/10.1016/j.optlastec.2016.09.003>
- [42] M. Z. Ge, J. Y. Xiang, L. Yang, J. T. Wang, Effect of laser shock peening on the stress corrosion cracking of AZ31B magnesium alloy in a simulated body fluid, *Surf. Coat. Technol.* 310 (2017) 157–165. <https://doi.org/10.1016/j.surfcoat.2016.12.093>
- [43] X. C. Li, Y. K. Zhang, J. F. Chen, Y. L. Lu, Effect of laser shock processing on stress corrosion cracking behaviour of AZ31 magnesium alloy at slow strain rate, *Mater. Sci. Technol.* 29 (2013) 626–630. <https://doi.org/10.1179/1743284712Y.0000000166>
- [44] M. Ascencio, M. Pekguleryuz, S. Omanovic, An investigation of the corrosion mechanisms of WE43 Mg alloy in a modified simulated body fluid solution: The influence of immersion time, *Corros. Sci.* 87 (2014) 489–503. <https://doi.org/10.1016/j.corsci.2014.07.015>
- [45] X. D. Ren, X. Q. Yang, W. F. Zhou, J. J. Huang, Y. P. Ren, C. C. Wang, Y. X. Ye, L. Li, Thermal stability of surface nano-crystallization layer in AZ91D magnesium alloy induced by laser shock peening, *Surf. Coat. Technol.* 334 (2018) 182–188. <https://doi.org/10.1016/j.surfcoat.2017.09.037>
- [46] P. Saha, M. Roy, M. K. Datta, B. Lee, P. N. Kumta, Effects of grain refinement on the biocorrosion and in vitro bioactivity of magnesium, *Mater. Sci. Eng. C* 57 (2015) 294–303. <https://doi.org/10.1016/j.msec.2015.07.033>
- [47] L. Yang, E. Zhang, Biocorrosion behavior of magnesium alloy in different simulated fluids for biomedical application, *Mater. Sci. Eng. C* 29 (2009) 1691–1696. <https://doi.org/10.1016/j.msec.2009.01.014>
- [48] J. H. Nordlien, S. Ono, N. Masuko, K. Nisancioglu, A TEM investigation of naturally formed oxide films on pure magnesium, *Corros. Sci.* 39 (1997) 1397–1414. [https://doi.org/10.1016/S0010-938X\(97\)00037-1](https://doi.org/10.1016/S0010-938X(97)00037-1)